RESEARCH PAPER

Modified smoothed particle hydrodynamics approach for modelling dynamic contact angle hysteresis

Yanyao Bao[1] · Ling Li[1] · Luming Shen[1] · Chengwang Lei[1] · Yixiang Gan[1]

Abstract

Dynamic wetting plays an important role in the physics of multiphase flow, and has a significant influence on many industrial and geotechnical applications. In this work, a modified smoothed particle hydrodynamics (SPH) model is employed to simulate surface tension, contact angle and dynamic wetting effects at meso-scale. The wetting and dewetting phenomena are simulated in a capillary tube, where the liquid particles are raised or withdrawn by a shifting substrate. The SPH model is modified by introducing a newly developed viscous force formulation at the liquid–solid interface to reproduce the rate-dependent behaviour of the moving contact line. Dynamic contact angle simulations with the interfacial viscous force are conducted to verify the effectiveness and accuracy of this new formulation. In addition, the influence of interfacial viscous forces with different magnitude on the contact angle dynamics is examined by empirical power-law correlations; the derived constants suggest that the dynamic contact angle changes monotonically with the interfacial viscous force. The simulation results are consistent with experimental observations and theoretical predictions, implying that the interfacial viscous force can be associated with the slip length of flow and the microscopic surface roughness. This work demonstrates that the modified SPH model can successfully account for the rate-dependent effects of a moving contact line, and can be used for realistic multiphase flow simulations under dynamic conditions.

Keywords Smoothed particle hydrodynamics · Contact angle dynamics · Capillary number · Interfacial viscous force

1 Introduction

Complex interactions among multiple phases (e.g. gas, liquid and solid) in porous media are of great significance in many industrial applications, such as groundwater treatment [1], oil recovery [2], carbon sequestration [3], unsaturated soil mechanics [4–6] and porous catalysts [7]. These processes usually involve dynamic wetting phenomena which are critical when describing the rate-dependent system properties, and can thus further shed light on optimisation of engineering solutions. Dynamic wettability is generally characterised by the dynamic contact angle. To access this property, previous studies focussed on experimental characterisation [8–10], theoretical modelling [11, 12] and various numerical approaches [13–15]. Numerical methods have demonstrated significant advantages in modelling multiphase flow [13,

15–17], including time and cost efficiency, a wide range of length scales, and broader ranges of material properties and loading conditions. However, to model dynamic wettability, most existing numerical approaches are either far from typical realistic time and length scales, e.g. molecular dynamics (MD) [16], or established based on the introduction of additional artificial interfacial constraints, e.g. smoothed particle dynamics (SPH) [15, 17].

Dynamic contact angles can be measured experimentally at the liquid–solid–vapour triple-line region in different ranges of the capillary number (Ca) [18, 19], a non-dimensional parameter defined as the ratio of viscous to interfacial forces:

$$Ca = \frac{\eta v_{\mathrm{t}}}{\gamma}, \tag{1}$$

where v_{t} is the triple-line region velocity, γ is the surface tension, and η is the viscosity of the fluid. The behaviour of the dynamic contact angle associated with motion of the contact line of a spreading liquid can be described using several theories, including hydrodynamic [11] or molecular-

✉ Yixiang Gan
   yixiang.gan@sydney.edu.au

1   School of Civil Engineering, University of Sydney, Sydney,
    NSW 2006, Australia

kinetics models [20], and their combination [21]. A number of empirical relationships based on these theoretical models for wetting have been discussed in literature, all of which express the dynamic advancing (or receding) contact angle θ_d^a (or θ_d^r) as a function of Ca and the corresponding quasi-static contact angle θ_s^a (θ_s^r) during the wetting (dewetting) process. For water on a glass or polyethylene plate, Elliot and Riddiford [22] found that the dynamic contact angle is rate independent when $Ca < 2 \times 10^{-7}$, whereas Schwartz and Tejeda [8] identified that the dynamic contact angle is constant for $Ca < 2 \times 10^{-6}$. For $10^{-6} < Ca < 10^{-2}$, the dynamic contact angle varies monotonically with Ca, where the most commonly suggested relationship is [23–25]

$$\left| \cos\theta_d^{a/r} - \cos\theta_s^{a/r} \right| = ACa^B, \tag{2}$$

where A and B are constants for the advancing/receding case. Based on a similar empirical correlation, Jiang et al. [9], Bracke et al. [10] and Seebergh and Berg [26] derived different constants for the proposed correlation, by introducing the additional term $1 / \left(1 + \cos\theta_s^{a/r} \right)$ on the right-hand side to minimise the deviation induced by fluid properties when comparing the results for different fluids. It has also been pointed out that the dependence of the contact angle on the velocity of the moving contact line, i.e. the value of B, is enhanced for rough surfaces [8, 26]. In addition, Kordilla et al. [27] and Shigorina et al. [28] studied droplet flow on smooth and rough surfaces under different flow conditions using a pairwise force (PF)-SPH model, and the resulting dynamic contact angles were validated against analytical and empirical solutions.

However, complete understanding of the dynamic contact angle associated with a moving contact line remains an open topic due to the complex liquid–solid interactions and the fundamental roles of the triple-line region in liquid spreading. Experimental investigations on the dynamic contact angle may be strongly influenced by small-scale physical and chemical heterogeneities, impurities adsorbed on the solid surface, growth and dissolution of bubbles etc. [29]. Therefore, considering the above-mentioned limitations and the availability of experimental conditions and facilities, numerical approaches, including MD [14, 16, 30, 31], the lattice Boltzmann method (LBM) [13, 32–35] and SPH [15, 17, 28], serve as powerful tools to study contact angle dynamics and the fundamental underlying mechanisms. At the micro-scale, Koplik et al. [14] identified rate-dependent behaviour for the dynamic receding angle using MD simulations of an immiscible two-fluid system. Meanwhile, Lukyanov and Likhtman [16] applied MD simulations to explain the behaviour of the dynamic contact angle from the perspective of the force

distribution and friction law. Furthermore, the atomic-scale microscopic characteristics of the contact line can be captured in MD simulations considering actual inter-particle potentials [36]. Nevertheless, MD simulations are mostly established on atomic scale and usually require high computing power. At the meso-scale (which usually refers to length scales from hundreds of micrometres to a few millimetres), researchers have also proposed and verified the power-law correlation between Ca and the dynamic contact angle for multiphase capillary flow using LBM and SPH models that agree with experimental and theoretical predictions [13, 15, 17, 32, 33]. Although the microscopic characteristics of the contact line force effect are inevitably oversimplified when using such coarse-grained approaches, an attempt has been made to develop a theoretical model to account for the surface tension and friction forces at the atomic length scale using LBM [37]. However, to deal with problems with moving boundaries, LBM algorithms must be modified, which worsens the accuracy of the standard scheme [38]. Recently, pairwise functions have been successfully introduced into SPH formulations to reproduce interfacial phenomena, including the surface tension and contact angle [39–41]. For the above-mentioned SPH models that were successfully used to simulate the dynamic contact angle, an additional term must be included, e.g. the contact line force formulation [15] or applying pairwise interaction forces with the dynamic Young–Laplace condition in the triple-line region [17], and they all assume a no-slip boundary condition, thus the effects of slip length on the contact angle dynamics have not yet been considered. We propose herein a modified SPH model to study the contact angle dynamics at meso-scale with pore sizes of around a millimetre. This SPH model adopts additional liquid–liquid and liquid–solid interaction forces to generate surface tension and wetting effects [42]. Moreover, to replicate realistic dynamic behaviour of liquid–solid interactions, an interfacial viscous force is introduced to capture viscous shearing, which was omitted from the original SPH formulation. This newly introduced interfacial force can recover the behaviour of a fluid on a rough surface based on a physically measurable quantity, i.e. the slip length, and the dependence of the resultant contact angle hysteresis on the slip length is demonstrated and verified. The advancing and receding contact angles are simulated in a capillary tube at various contact line speeds. By analysing the correlations between the contact line velocity and contact angle, empirical power-law correlations with various constants are obtained. Furthermore, parametric studies are conducted to demonstrate that these predicted dynamic behaviours correlate with the proposed interfacial viscous force model.

2 SPH model

2.1 Governing equations

The motion of an incompressible fluid is governed by the Navier–Stokes equations, which can be written in Lagrangian form as follows:

$$\frac{d\rho}{dt} = -\rho \nabla \cdot \boldsymbol{v}, \tag{3}$$

$$\frac{d\boldsymbol{v}}{dt} = -\frac{\nabla P}{\rho} + \mu \frac{\nabla^2 \boldsymbol{v}}{\rho} + \boldsymbol{F}, \tag{4}$$

where ρ is the fluid density, $\boldsymbol{v}$ is the flow velocity, P is the pressure, $\mu \frac{\nabla^2 \boldsymbol{v}}{\rho}$ is the viscous term, and $\boldsymbol{F}$ corresponds to the total volumetric force acting on unit mass. In this study, Young–Laplace boundary conditions are not included, as in previous work [17, 27, 28].

We approximate the incompressibility of the fluid using a weakly compressible approach, applying an equation of state (EOS) in the form [43]

$$P = \frac{c^2 \rho_0}{\chi} \left[\left(\frac{\rho}{\rho_0} \right)^\chi - 1 \right], \tag{5}$$

where c is an artificial speed of sound, ρ_0 is a reference density, and χ is an empirical parameter. In this work, we choose the artificial speed of sound to be $c > 10 V_{\max}$ along with $\chi = 7$ [44, 45], where $V_{\max}$ is the expected maximum particle velocity.

2.2 SPH equations

The SPH method is based on the idea that a continuous field $A(\boldsymbol{r}_i)$ at position $\boldsymbol{r}_i$ can be smoothed by a convolution integral with a smoothing function $W(\boldsymbol{r}_i - \boldsymbol{r}_j, h)$, which allows the value of any function to be obtained at a given point as [46]:

$$A(\boldsymbol{r}_i) = \sum_{j=1}^{N} \frac{m_j}{\rho_j} A(\boldsymbol{r}_j) W(\boldsymbol{r}_i - \boldsymbol{r}_j, h), \tag{6}$$

where the summation is over N neighbouring particles around the specified particle $\boldsymbol{r}_i$, and m_j, $\boldsymbol{r}_j$, ρ_j are the mass, position and local density of particle j, respectively, $W(\boldsymbol{r}_i - \boldsymbol{r}_j, h)$ is the smoothing function with smoothing length of h. The following Gaussian kernel is adopted for the proposed SPH model, considering both calculation accuracy and computational efficiency [47]:

$$W(\boldsymbol{r}, h) = \frac{1}{h\sqrt{\pi}} e^{-\left(\frac{r^2}{h^2} \right)}. \tag{7}$$

The density of a liquid particle i is evaluated as

$$\rho_i = \sum_j m_j W(\boldsymbol{r}_i - \boldsymbol{r}_j, h). \tag{8}$$

The pressure-driven part of the momentum equation is implemented following the approach proposed by Monaghan [46], where the pressure gradient is symmetrised by rewriting $\nabla P / \rho$ in Eq. (4) to ensure momentum conservation:

$$\nabla P_i = \rho_i \sum_j m_j \left(\frac{P_i}{\rho_i^2} + \frac{P_j}{\rho_j^2} \right) \nabla W(\boldsymbol{r}_i - \boldsymbol{r}_j, h). \tag{9}$$

A Monaghan-style artificial viscosity model [46] is applied to stabilise the numerical algorithm. The artificial viscosity is obtained by writing the momentum equation in the form

$$\mu \frac{\nabla^2 \boldsymbol{v}_i}{\rho_i} = -\sum_j m_j \Pi_{ab} \nabla W(\boldsymbol{r}_i - \boldsymbol{r}_j, h), \tag{10}$$

where Π_{ab} is given by

$$\Pi_{ij} = \begin{cases} \frac{-\alpha \bar{c}_{ij} \mu_{ij} + \beta \mu_{ij}^2}{\bar{\rho}_{ij}}, & \boldsymbol{v}_{ij} \cdot \boldsymbol{r}_{ij} < 0, \\ 0, & \boldsymbol{v}_{ij} \cdot \boldsymbol{r}_{ij} > 0 \end{cases} \tag{11}$$

and

$$\mu_{ij} = \frac{h \boldsymbol{v}_{ij} \cdot \boldsymbol{r}_{ij}}{\boldsymbol{r}_{ij}^2 + 0.01 h^2}, \tag{12}$$

where α and β are constants, $\bar{c}_{ij} = (c_i + c_j)/2$, and $\bar{\rho}_{ij} = (\rho_i + \rho_j)/2$ are the values of the sound speed and the density averaged between particles i and j. It was suggested by Monaghan [46] that values of α and β of 1 and 2, respectively, give the best results. In this work, we adopt this value for α, but set the value of β to 0, as the motion of the fluid flow in the simulation is relatively slow (ranging from 0.0002 to 20 mm/s). Note that the implementation of this artificial viscosity could lead to unphysically high shear viscous forces, because SPH simulations are stabilised by the physical viscosity of the fluid, and it is challenging to simulate low-viscosity flows [48]. Therefore, our simulations are carried out with this highly viscous setting.

For the weakly compressible SPH formulation, the time step Δt in this work follows the Courant–Friedrichs–Lewy (CFL) condition based on: (1) the maximum artificial sound speed and the maximum flow speed, (2) the magnitude of the particle acceleration f_i and (3) the viscous condition [42].

2.3 Implementation of the inter-particle force model in SPH

Generally, two approaches are used to prescribe the surface tension and contact angle in SPH models. The first approach

is the continuum surface force method proposed by Brackbill et al. [49]. The second is the pairwise force model introduced by Tartakovsky and Meakin [39], later extended to different forms of pairwise forces [17]. In this work, an inter-particle force formulation [41] adopted from dissipative particle dynamics (DPD) [40] is applied to reproduce the surface tension and wetting effects. The pair potential energy $U(r)$ and inter-particle force $\boldsymbol{F}_{ij}^{\text{inter}}$ are given as

$$U(r) = \alpha_{ij}\big[CW^{\text{e}}(r, h_1) - DW^{\text{e}}(r, h_2)\big], \quad h_1, h_2 \leq 0.5\,h, \quad (13)$$

$$\boldsymbol{F}_{ij}^{\text{inter}} = -\frac{\mathrm{d}U(r)}{\mathrm{d}r}\frac{\boldsymbol{r}_i - \boldsymbol{r}_j}{\|\boldsymbol{r}_i - \boldsymbol{r}_j\|}, \quad i \neq j, \quad (14)$$

where α_{ij} is the inter-particle force strength parameter, C and D are constants, and W^{e} is the cubic spline function to construct the potential energy function with the form

$$W^{\text{e}}(r, h) = \begin{cases} 1 - \frac{3}{2}\left(\frac{r}{h}\right)^2 + \frac{3}{4}\left(\frac{r}{h}\right)^3, & 0 < \frac{r}{h} \leq 1, \\ \frac{1}{4}\left(2 - \frac{r}{h}\right)^3, & 1 < \frac{r}{h} \leq 2, \\ 0, & \text{otherwise.} \end{cases} \quad (15)$$

This kernel function W^{e} is normalised by $\frac{2}{3h}$, $\frac{10}{7\pi h^2}$ and $\frac{1}{\pi h^3}$ in one-dimensional (1D), two-dimensional (2D) and three-dimensional (3D) space, respectively. The inter-particle force in Eq. (14) is added into the SPH momentum conservation equation, and imposed on both liquid and solid particles to generate multiphase interactions between different phases. The parameter α_{ij} is replaced by α_1 (as the liquid–liquid interaction force parameter) when particle j is a liquid particle and by α_2 (liquid–solid interaction force parameter) when particle j is a solid particle. Note that particle i is always a liquid particle. By assigning different values for α_1 and α_2, different values of the surface tension of a free surface and the static contact angle on a solid surface can be reproduced in the simulation. In addition, to prevent unphysical penetration of liquid particles into solid particles, additional repulsive boundary forces are implemented, similar to those implemented in Ref. [50].

2.4 Modified liquid–solid interface model

In most SPH simulations, the boundaries of rigid bodies are prescribed using different mechanisms such as ghost particles [51], normalising conditions [52] or boundary particle forces [50], all of which are only appropriate for perfectly smooth boundaries [53]. Considering the particle–particle interaction force at a liquid–solid interface, the sum of the short-range repulsive and longer-range attractive forces acting on a liquid particle fluctuates around zero in the tangential direction, which effectively makes the interface frictionless and rate independent (Fig. 1b). In addition to the absence of

viscous shearing between the liquid and solid phases, as a Monaghan-style artificial viscosity is used in this work, the rate-dependent behaviour of a moving contact line is hardly achieved in this circumstance.

Several approaches can be used in SPH to prescribe the dynamic contact angle at a contact line, as previously discussed. However, the above approaches assume no-slip boundary conditions, thus the effects of the slip length on the contact angle dynamics are not considered. It is also feasible to implement the Navier–Stokes equations using a Navier-slip boundary condition or an empirical law for the contact angle dynamics, while the physical characteristics of the solid–liquid interface, including the slip length and surface roughness, can be omitted. In this work, we introduce a new algorithm which imposes a viscous force $\boldsymbol{F}_{ij}^{\text{vis}}$ on the liquid particles based on the actual shearing at the liquid—solid interface, to reproduce the rate-dependent behaviour of the moving contact line. In Refs. [17, 27, 28], the momentum conservation equation is subjected to the Young–Laplace boundary condition at the interfacial region, thus reproducing also the contact angle dynamics. Here, we focus on reproducing the dynamic contact angle effects, considering the slip length at the solid–liquid interface. For an ideal no-slip condition, the tangential force between the solid and liquid can be expressed as

$$\boldsymbol{F}_{ij}^{\text{vis}} = -S \cdot \tau \cdot \boldsymbol{t} = -L_0 \cdot \eta \cdot \dot{\gamma} \cdot \boldsymbol{t} = -L_0 \cdot \eta \cdot \frac{\Delta \boldsymbol{v}^{\text{t}}}{L_0/2}, \quad (16)$$

where S is the liquid–solid contact area (becoming for a two-dimensional case the particle spacing L_0), τ is the shear stress, η is the viscosity of the bulk fluid, $\dot{\gamma}$ is the shear rate, $\boldsymbol{t}$ is the tangential unit vector, and $\Delta \boldsymbol{v}^{\text{t}}$ is the relative tangential velocity between liquid and solid particles. The thickness of shearing equals half the interface spacing L_0, as shown in Fig. 1a. This formulation is based on the assumptions of laminar flow with a constant shear rate and a no-slip boundary condition at the liquid–solid interface.

Experimental studies report a slip length ranging from 10 nm to 10 µm for various surfaces and liquids [54–57]. However, compared with predictions under no-slip boundary conditions with the bulk fluid viscosity, the average boundary fluid velocity and slip length of pressure-driven flow can increase dramatically on certain surfaces, such as superhydrophobic and rough surfaces [58–61]. For example, the slip length can reach hundreds of nanometres for hexadecane flowing over a bare sapphire surface [58], up to 400 µm on hydrophobic micro–macro structures [61] and even larger than 1 mm for fluid flow through an aligned carbon nanotube membrane [60]. In addition, MD simulations also suggest that the slip length may increase for fluids at the triple-line region [14].

To take the presence of the slip length into account, the interfacial force formulation in Eq. (16) must be modified.
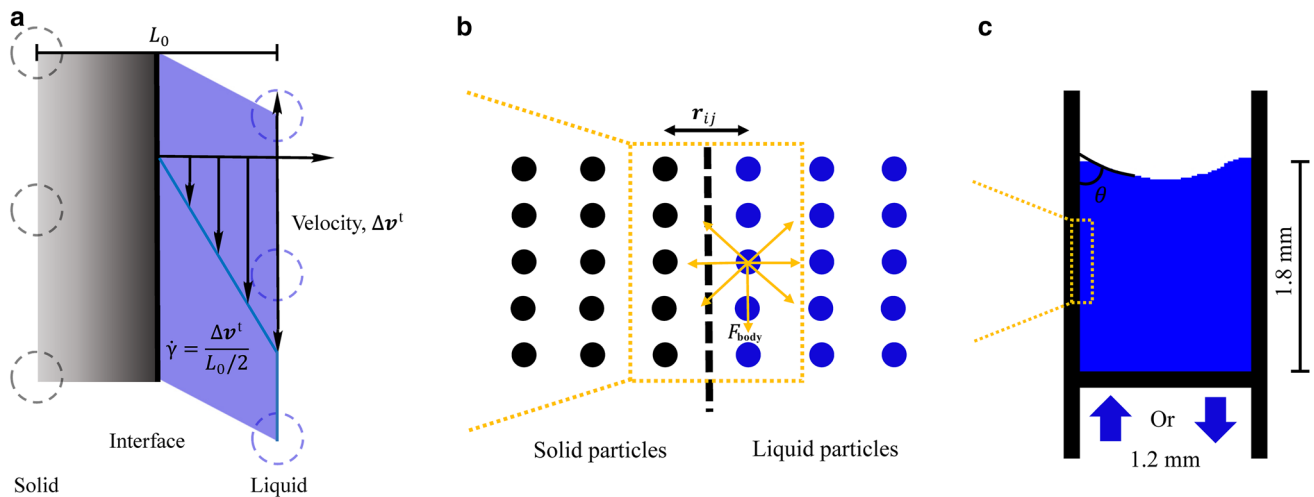
Fig. 1 Schematics of the modified SPH approach (not to scale): **a** shearing between solid and liquid particles at liquid–solid interface; **b** force balance of liquid particle; **c** geometry of capillary tube for dynamic contact angle simulation

Figure 2 illustrates the equivalent model for an effective shear rate $\dot{\gamma}^*$, considering a slip boundary condition with slip length of L_s. The equivalent model should have the same tangential force as the actual case with a slip condition, thus

$$F_{ij}^{\text{vis}} = -L_0 \cdot \eta^* \cdot \frac{\Delta \boldsymbol{v}^{\text{t}}}{L_0/2} = -L_0 \cdot \eta \cdot \frac{\Delta \boldsymbol{v}^{\text{t}}}{L_0/2 + L_s}, \tag{17}$$

where η^* is the equivalent viscosity, or apparent viscosity, at the interface. Thus, we have

$$\eta^* = \eta \cdot \frac{L_0}{L_0 + 2L_s}. \tag{18}$$

Therefore, the bulk viscosity η at the interface is replaced by a smaller value η^* ($L_s > 0$) to reproduce the actual shear profile at the liquid–solid interface. Finally, the interfacial viscous force F_{ij}^{vis} is added to the inter-particle force formulation in the form

$$F_{ij}^{\text{vis}} = \begin{cases} -L_0 \cdot \eta^* \cdot \frac{\Delta \boldsymbol{v}^{\text{t}}}{L_0/2}, & r_{ij} \le L_0, \\ 0 & r_{ij} > L_0. \end{cases} \tag{19}$$

Mesh sensitivity studies suggest that the use of Eqs. (18) and (19) is independent of the particle spacing L_0. After this modification with the inter-particle interaction force, F_{ij}^{inter}, and interfacial viscous force, F_{ij}^{vis}, the SPH discretisation of the governing equation now reads

$$\frac{\mathrm{d}\boldsymbol{v}_i}{\mathrm{d}t} = -\sum_j m_j \left[\frac{P_i}{\rho_i^2} + \frac{P_j}{\rho_j^2} + \Pi_{ab} \right] \nabla W(\boldsymbol{r}_i - \boldsymbol{r}_j, h)$$
$$+ \boldsymbol{g} + \sum_j \frac{F_{ij}^{\text{inter}}}{m_i} + \sum_j \frac{F_{ij}^{\text{vis}}}{m_i}. \tag{20}$$

This SPH model is implemented in the PySPH open-source framework [62]. The parameters used in this work are listed in Table 1, unless otherwise mentioned.
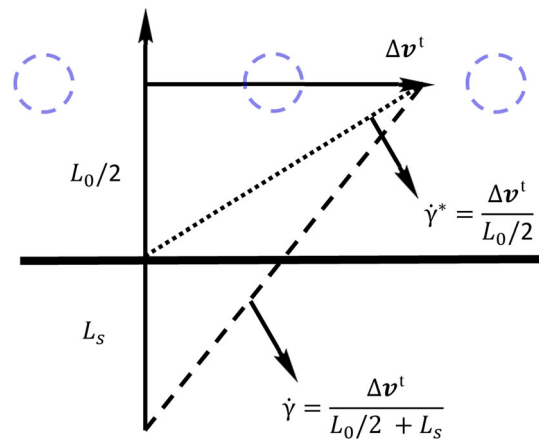
Fig. 2 Velocity profiles and shear rate for slip condition (dashed line) and equivalent no-slip condition (dotted line)

3 Results and discussion

3.1 Identification of model parameters

To examine the surface tension scheme used in this study, the shape evolution of a 2D droplet with zero gravity in vacuum is presented. The equilibrated average density of the droplet is 997 kg/m^3, based on the bulk region of the droplet. Figure 3a shows the shape transformation of the droplet from a square to circle due to the surface tension effect. The surface tension γ can be calculated using the Young–Laplace equation, which relates the difference between the internal and external pressure of the droplet ΔP and its radius R as

$$\gamma \left(\frac{1}{R_1} + \frac{1}{R_2} \right) = \Delta P, \tag{21}$$

Table 1 Parameters for dynamic contact angle simulations

Parameter	Symbol	Value
Density (kg/m^3)	ρ_0	997
Gravity (m/s^2)	g	9.8
Viscosity (Pa·s)[a]	η	0.013, 0.04, 0.185
Interfacial viscosity (Pa·s)	η^*	0.0006–0.009
Slip length (μm)[b]	L_s	100–1000
Surface tension (N/m)[a]		0.28
Particle mass (kg)	m_0	6.25×10^{-7}
Particle spacing (m)	L_0	2.5×10^{-5}
Smoothing length (m)	h	7.5×10^{-5}
Artificial sound speed (m/s)	c	3.0
Time step (s)	Δt	4.15×10^{-7}
Liquid–liquid interaction force parameter (J)	α_1	5.42×10^{-4}
Liquid–solid interaction force parameter (J)	α_2	5.69×10^{-4}

[a]These material properties are the results of other input parameters
[b]The values here correspond to the interfacial viscosity used in the simulations

where R_1 and R_2 are the principal radii of curvature of the droplet. Since the air phase is not explicitly modelled due to limited computational resources, ΔP here equals the pressure inside the droplet and the mean radius equals the droplet radius R. In this work, the total pressure of the droplet results from the combined contributions of both the EOS and the inter-particle force F_{ij}^{inter} [41]. Due to the boundary deficiency [63], we exclude the edge of the droplet and use the bulk region for the pressure measurement. Seven tests are conducted with different values of α_1 ranging from 2.0×10^{-5}

to 5.5×10^{-4} J. The results suggest a linear relationship between α_1 and γ (Fig. 3b).

The liquid–solid interaction strength parameter α_2 is calibrated by simulating six different equilibrium contact angles for a droplet over a flat substrate, with thickness of 0.1 mm, as shown in Fig. 4a. The droplet has a volume of 2.5 mm^3, and it is slowly brought into contact with the flat surface by a gravity force. After the droplet reaches equilibrium (after approximately 0.25 s), the curvature of the droplet at the triple-line region is fitted using a circle. Then, a tangent line is drawn at the intersection of the circle and substrate. The included angle between the tangent line and substrate is measured as the static contact angle. Figure 4 shows that different wetting behaviours from hydrophobicity to hydrophilicity can be simulated by adjusting the liquid–solid interaction strength parameter α_2.

3.2 Dynamic contact angle

To simulate a moving contact line and the dynamic contact angle, a 2D capillary tube with a shifting substrate is modelled in vacuum with the following geometry and parameters: The size of the capillary tube is 4 mm × 1.36 mm, containing fluid in a domain of 1.8 mm × 1.2 mm, as shown in Fig. 1c. The surface tension and bulk viscosity of the simulated fluid are fixed unless otherwise mentioned, and Ca is only controlled by the triple-line velocity, v_t, in this work. To measure the dynamic contact angle, the simulation process is recorded and snapshots of the simulation domain are taken every 100 time steps after the wetting front becomes stable. The first three layers of liquid particles adjacent to the solid boundary are excluded from the contact angle measurement, because the triple-line region becomes less resolvable due to the weak compressibility, particle spacing and strong
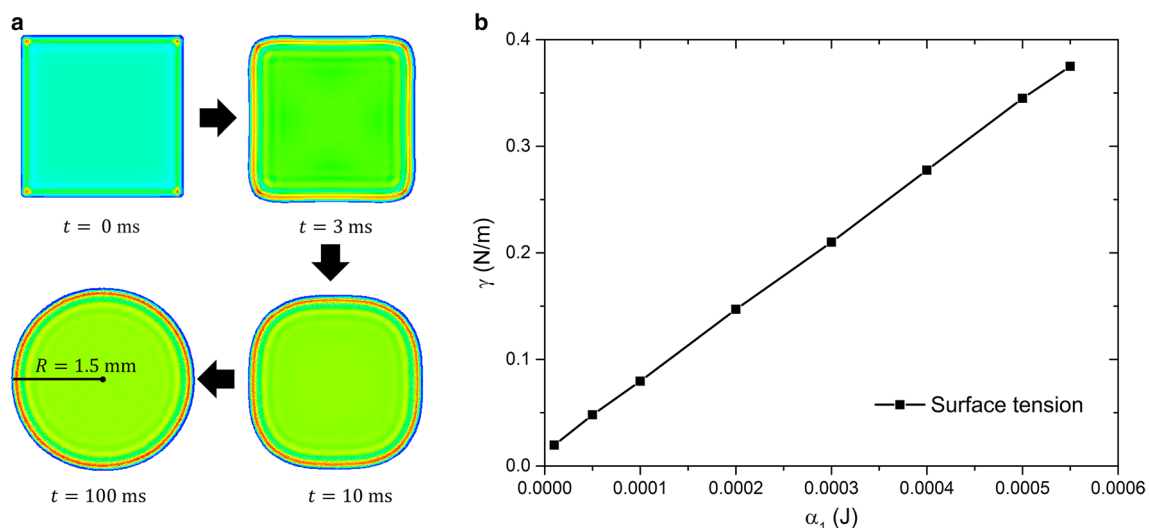
**Fig. 3** **a** Evolution of droplet shape. **b** Surface tension with different values of α_1
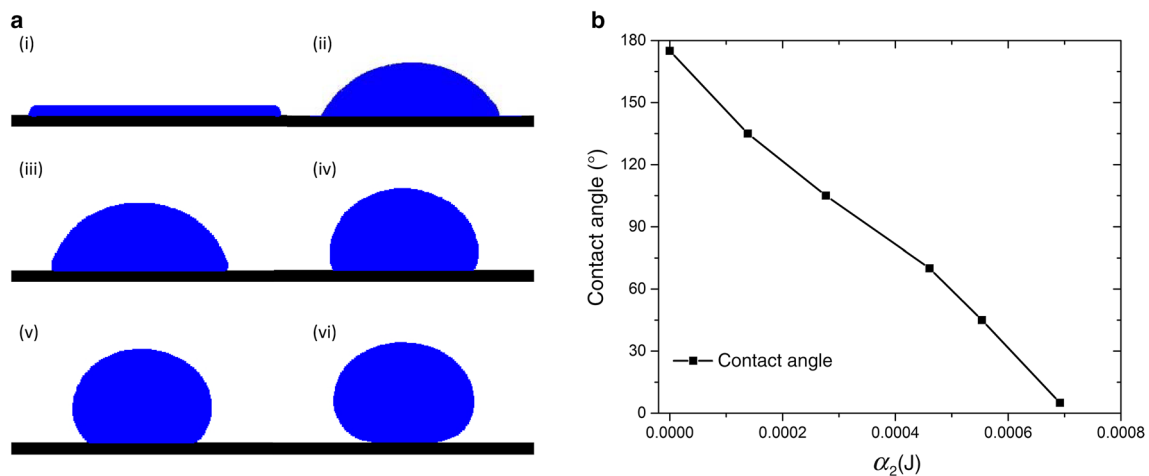
Fig. 4 a Static contact angles for different values of α_2. **b** Relation between static contact angle and α_2

solid–liquid interaction force that results in frequent reconstruction of the liquid particles. Note that this boundary effect could be overcome by simulations with sufficient resolution. Then, the flow curvature at the triple-line region is fitted using a circle, followed by drawing a tangent line at the intersection of the solid boundary and the circle. The dynamic contact angle θ_d is considered to be the included angle between the solid boundary and the tangent of this fitted circle.

Prior to the simulations with different substrate moving speeds, the capillary tube is in the same stable configuration in terms of fluid curvature and static contact angle. In all the simulations, the bottom substrate moves along the y-direction for a distance of 1.2 mm to raise or withdraw the fluid with various velocities to generate a moving contact line. Figure 5 shows snapshots of the fluid movement and curvature at different simulation time steps. The advancing angle occurs when the fluid is pushed up, while the receding angle is formed when the substrate withdraws the fluid. At any given time, the resulting contact angle is recorded against the instantaneous contact line speed.

Figure 5 shows five snapshots of the capillary tube with the substrate moving at a velocity of 10 mm/s at simulation times of 0 ms, 5 ms, 25 ms, 60 ms, and 80 ms. At the beginning of the simulation, due to the weak compressibility and low sound speed of the simulated fluid, it takes hundreds of time steps for the substrate to transfer its speed to all the liquid particles. Subsequently, the fluid curvature starts to change and the advancing (or receding) angle keeps increasing (or decreasing) from simulation time of 0 ms to 60 ms. After 60 ms, the fluid curvature becomes stable, and the contact angle measurement is conducted thereafter. Note that the velocity of the substrate does not necessarily equal the velocity of the triple-line region, and the position and velocity of the liquid particles are updated according to the smoothing function at each time step, so the fitted contact angle and Ca
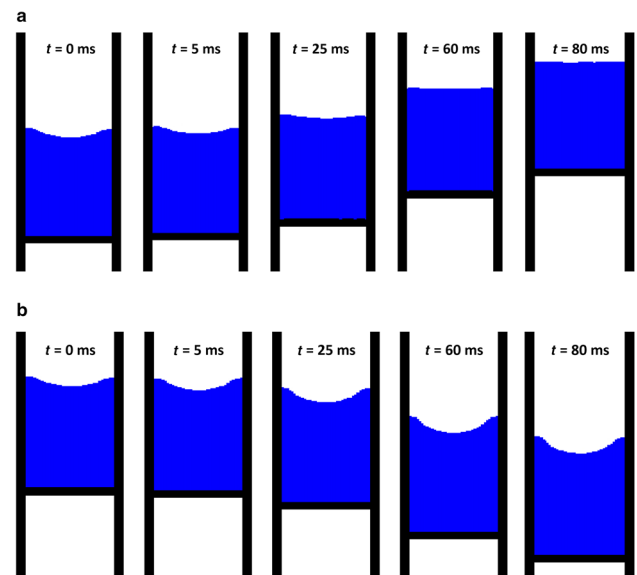
Fig. 5 Snapshots of dynamic contact angle simulations at various times with the substrate moving at 10 mm/s: **a** advancing case; **b** receding case

will vary during the simulation. Therefore, when the curvature becomes stable, i.e. after simulation time of 60 ms in this case, hundreds of sets of contact line velocities and dynamic contact angles are recorded for subsequent data processing and analysis.

To examine the effect of the proposed interfacial viscous force, we conducted two dynamic contact angle simulations, implemented with and without the term F_i^{vis} (more specifically, $\eta^* = 0.003$ Pa·s and $\eta^* = 0$ Pa·s, respectively); the results in terms of the dynamic contact angle are compared in Fig. 6. Both cases are simulated for 12 substrate moving speeds ranging from 0.002 to 20 mm/s. The resulting Ca ranges from 10^{-6} to 10^{-1}.
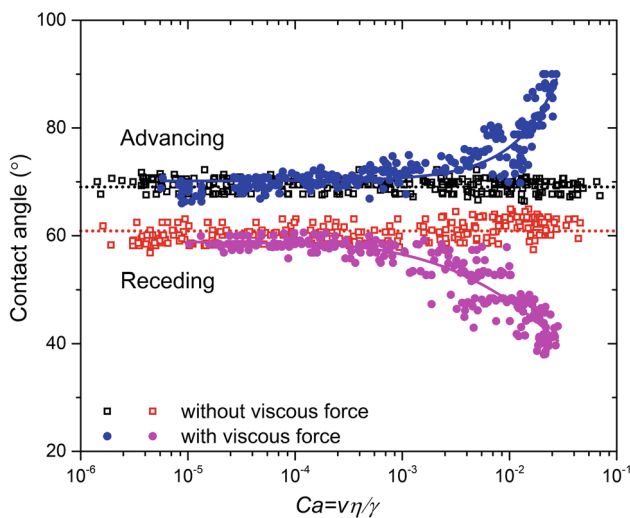
Fig. 6 Scatter plot of dynamic contact angle simulations with and without interfacial viscous force, F_i^{vis}. Blue and pink circles represent advancing and receding cases with F_i^{vis}, respectively; Black and red squares represent advancing and receding cases without F_i^{vis}. Trend lines serve as a guide to the eye

For $Ca < 10^{-4}$, the dynamic contact angle simulation results are independent of F_i^{vis}, with dynamic advancing and receding angle of around 70° and 60°, respectively. For $10^{-4} < Ca < 10^{-3}$, slight differences can be observed in the results. For the cases implemented with F_i^{vis}, the dynamic advancing angle starts to increase and the receding angle starts to decrease, while the dynamic contact angle remains unchanged in the case without F_i^{vis}. The major difference occurs in the large-Ca regime ($Ca > 10^{-3}$): with the increase of Ca, the dynamic advancing/receding contact angle remains almost constant in the case without F_i^{vis}, which suggests there is no rate-dependent behaviour of the dynamic contact angle. This is because the Young–Laplace boundary condition is not explicitly prescribed in this study, and the applied Monaghan-style artificial viscosity does not reproduce viscous shearing between different phases. Meanwhile, for the cases implemented with F_i^{vis}, the dynamic advancing angle increases from 70° to around 90° while the dynamic receding angle decreases from 60° to less than 40° as Ca approaches 0.02.

These simulation results suggest that the interfacial viscous force formulation is key for reproducing the dynamic contact angle. According to Eq. (19), the interfacial viscous force F_i^{vis} at the liquid–solid interface region increases with the velocity of the liquid particles. Therefore, the F_i^{vis} formulation will result in a different influence on the motion of the moving contact line depending on the magnitude of the triple-line velocity, v_t. In the case where v_t is relatively small ($Ca < 10^{-4}$), the magnitude of the interfacial viscous force F_i^{vis} is also negligible and contact angle hysteresis is hardly observed within the small-Ca regime. When v_t becomes

larger, F_i^{vis} starts to influence the behaviour of the moving contact line. In such a circumstance, the relative motion of the contact line is restricted and slowed down along the flow direction. Meanwhile, the bulk fluid in the middle region of the capillary tube is not affected by the interfacial viscous force. Hence, this part of the fluid moves quicker than the fluid in the triple-line region, which creates a larger (or smaller) contact angle for the advancing (or receding) case. In summary, when adopting the newly introduced interfacial viscous force formulation, the proposed SPH model can successfully simulate the dynamic contact angle.

In the following, empirical power-law correlations are used to examine the results, similar to the format of the "universal function" [26]. The above simulation results with the inclusion of F_i^{vis} are replotted in Fig. 7 using a smoothed density histogram plot. Note that the legend bars represent the relative probability densities; e.g. "1.0" refers to the highest density. Then, the power-law correlation of Eq. (2) is used to fit the results, and the constants are derived. From previous studies, we know that the exponent B ranges from 0.2 to 1.0 based on various experimental findings and theoretical predictions [23]. In our simulation results with $\eta^* = 0.003$ Pa·s, B values of 0.531 and 0.406 are derived for the advancing and receding cases, respectively. Later in Sect. 3.3, we further examine the dependence of η^* for both the exponent and amplitude constants. Here, the quasi-static advancing and receding contact angles ($\theta_s^a = 69.53°$ and $\theta_s^r = 59.82°$) are obtained by raising or lowering the bottom substrate at an extremely slow velocity of 2×10^{-5} mm/s.

3.3 Influence of η^*

This section presents a parametric study on the interfacial viscous force F_i^{vis} formulation, i.e. η^*. Recall that η^* is the only parameter in the simulation for both the advancing and receding loading paths, and the represented slip length (L_s) is a measurable quantity from physical experiments. To study the correlation between the interfacial viscous force parameter η^* and the resulting dynamic contact angle, six sets of simulations with η^* of 0, 0.0006, 0.0015, 0.003, 0.006 and 0.009 Pa·s are conducted. The receding case with $\eta^* = 0.009$ Pa·s is not shown due to the strong adhesion between the liquid and solid phase, which is explained later in this section. Each set of simulations are conducted with different substrate speeds, resulting in Ca ranging from 10^{-6} to 10^{-2}.

We select the simulations with bottom substrate speed of 20 mm/s, 10 mm/s, 2 mm/s, 0.2 mm/s, 0.02 mm/s and 0.002 mm/s to study the correlation between the dynamic contact angle and Ca with different η^* values. Figure 8 shows that larger η^* results in a larger advancing angle and smaller receding angle, especially in the higher Ca region, which means that the contact angle hysteresis is enhanced with the increase of η^*. As Ca gets smaller, the dynamic advancing
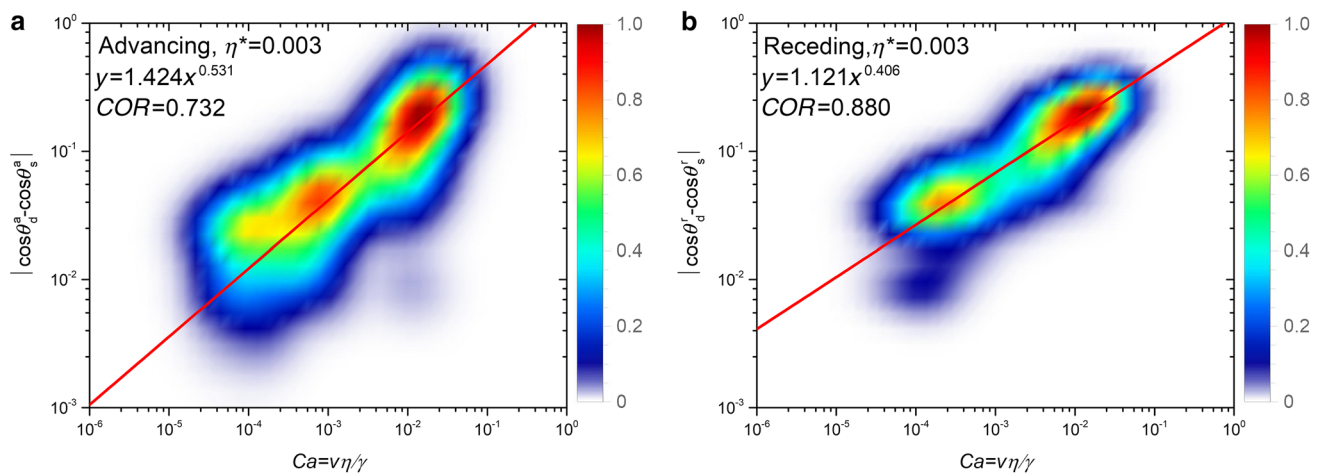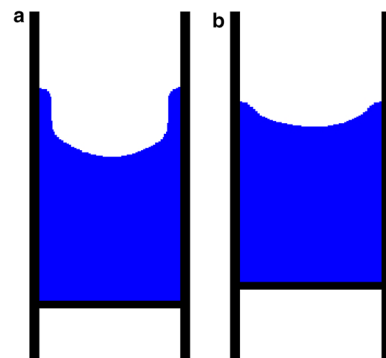
Fig. 7 Density histogram plots and power-law fitting for dynamic **a** advancing and **b** receding contact angle results; x and y correspond to Ca and $\left|\cos\theta_d^{a/r} - \cos\theta_s^{a/r}\right|$, respectively. COR is the correlation coefficient of the fit
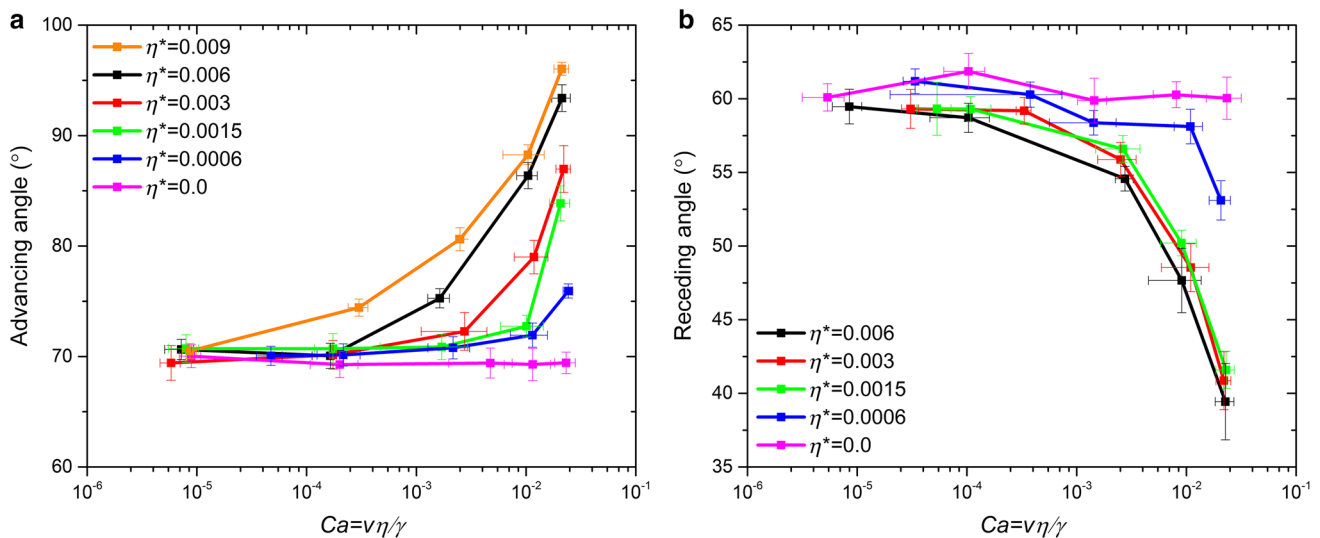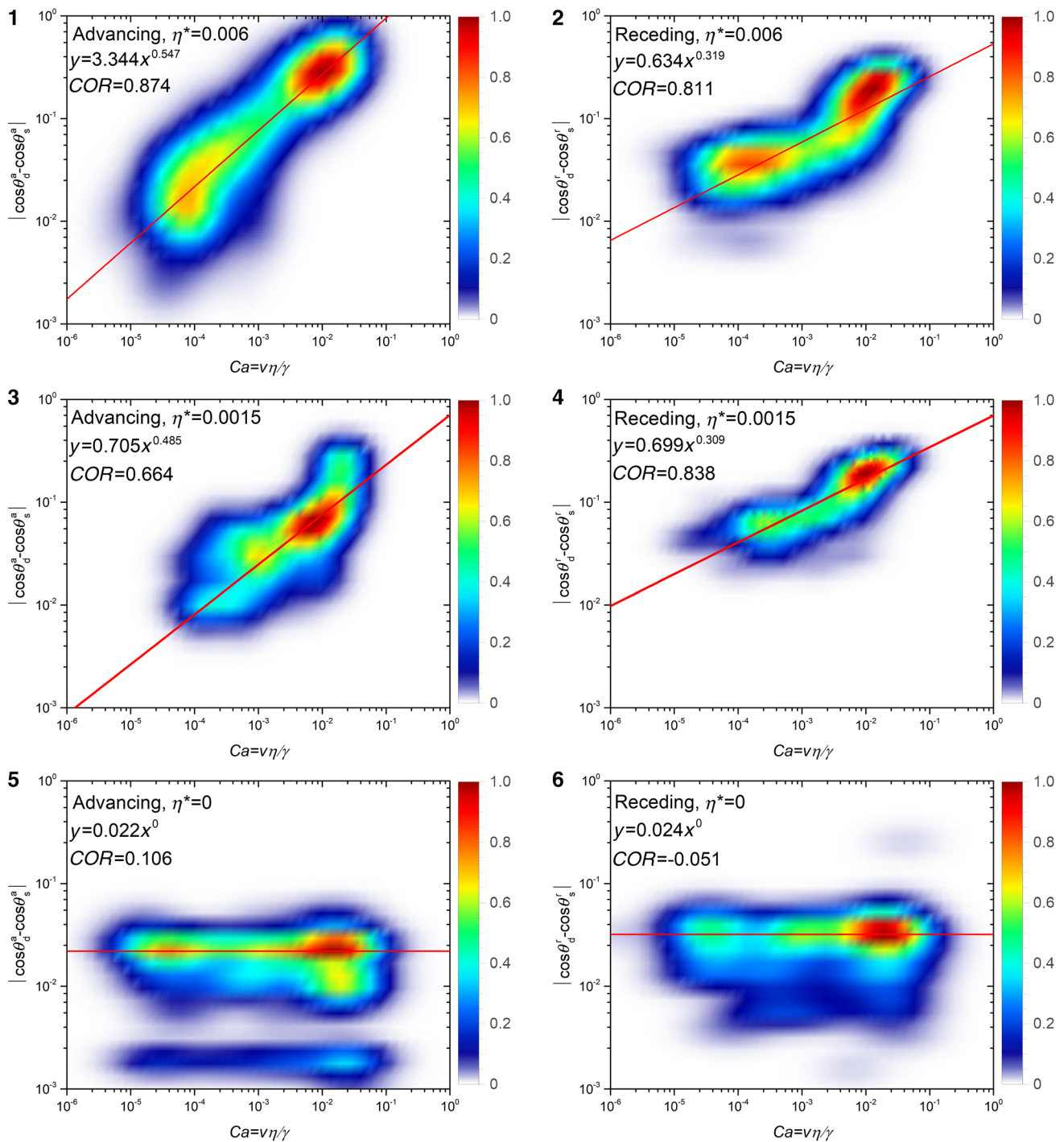

Fig. 8 Dynamic contact angle with different magnitudes of interfacial viscous force for **a** advancing and **b** receding cases

and receding angle converge to around 70° and 60°, respectively.

The enhancement of the dynamic contact angle for larger η^* can be interpreted from the perspective of the slip length and surface roughness, and this phenomenon is in good agreement with experimental results. Existing analytical models reveal that the real surface roughness is an important microscopic parameter controlling the slip length at the interface [64]. MD simulations report a significant reduction of the effective slip length in the presence of periodic surface roughness [65], and a general nonlinear relationship between the slip length and the local shear rate has been identified at a solid roughness surface [66]. Previous SPH simulations considered droplet movement on rough surfaces, although the correlation between the slip length and roughness is not fully revealed [27, 28]. In addition, rough surfaces were found to

Fig. 9 Dynamic receding angle simulations with $\eta^* = 0.006$ Pa·s: **a** presence of a thin water film for a substrate moving at 20 mm/s; **b** no thin water film when the substrate moves at 2 mm/s

Fig. 10 Density histogram plots and power-law fitting for dynamic contact angle results with different η^* values ($\eta^* = 0.006$, 0.0015 and 0 Pa·s); x and y correspond to $\left|\cos\theta_s^{a/r} - \cos\theta_d^{a/r}\right|$ and Ca, respectively

enhance the contact angle hysteresis in experimental study of the spreading of polyethylene glycol on rough hydrophobic surfaces [67]. According to Eq. (18), the value of η^* is inversely proportional to the slip length L_s in the model. Therefore, the selection of a relatively large value of η^* corresponds to a small L_s, representing a rough surface, and such

a surface is observed to have relatively large contact angle hysteresis, consistent with the experimental observations.

Nevertheless, in the receding case when η^* is larger than 0.0015 Pa·s, the dynamic angles in the high-Ca regime are less dependent on the actual value of η^*. The limited simulation resolution and number density as well as the strong
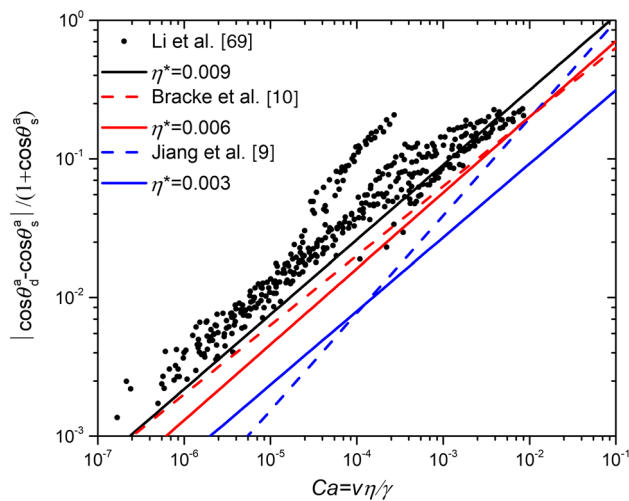
Fig. 11 Comparison of power-law correlations obtained from simulations with experimental data and empirical power-law correlations

liquid–solid particle interactions are considered to be responsible for this existence of seemingly unrealistic liquid film, albeit at a much lower scale, similar to the presence of a Landau–Levich film [68]. In scenarios with relatively large F_i^{vis}, a thin water film is formed and attached to the solid surface, such that the gravity force can hardly drive it downwards (Fig. 9a). In such a case, the dynamic receding angle is perceived as the intersection between the water film and fluid curvature, and the angles converge for $\eta^* = 0.0015$, 0.003 and 0.006 Pa·s. When the velocity of the moving contact line is lower, or F_i^{vis} is less significant, no water film forms on the solid surface, as shown in Fig. 9b.

To obtain further understanding of how the parameter η^* influences the dynamic contact angle, the simulation results obtained with five different values of η^* are fitted with Eq. (2), and the corresponding amplitude A and exponent B derived. In Fig. 10, it is observed that A and B in the power-law fit

change with the value of η^* (only limited cases are shown due to space restrictions). For $\eta^* \geq 0.0015$ Pa·s, the slope is quite obvious: the value of $\left|\cos\theta_d^{a/r} - \cos\theta_s^{a/r}\right|$ increases with the increase of Ca. For the case $\eta^* = 0$, the slope is 0 as expected, since there is no rate-dependent behaviour of the contact angle.

Furthermore, we compare our numerical predictions using $\eta^* = 0.009$, 0.006 and 0.003 Pa·s with the empirical power-law correlations proposed in Refs. [9, 10] and experimental data extracted from Ref. [69] that include various combinations of liquid and solid materials. Since all these previous studies focussed on the dynamic advancing case for various types of liquid, we use here the additional term $\left(1 + \cos\theta_s^a\right)$ to unify the numerical and experimental data, as shown in Fig. 11. Excellent agreement is observed between the simulation results with $\eta^* = 0.009$ Pa·s and the experimental data from Ref. [69]. In addition, the simulation results using $\eta^* = 0.006$ Pa·s and $\eta^* = 0.003$ Pa·s are consistent with the empirical correlations derived by Jiang et al. [9] and Bracke et al. [10], respectively. Note that, instead of fitting the experimental data using two-parameter power-law correlations, our prediction only depends on the value of the interfacial viscosity η^*, which has a physical meaning as shown in Eq. (18) and can be identified independently from measurements of the apparent slip length. This verification of our simulation results demonstrates that not only can the model reproduce the rate-dependent behaviour of a moving contact line but also good agreement with existing experimental studies can be achieved.

All the fitting results for A and B, viz. the amplitude and exponent, respectively, for different magnitudes of η^* are plotted in Fig. 12. In general, the values of A and B increase with η^*. The only exception is the dynamic receding angle with $\eta^* = 0.006$ Pa·s. The reason is again the formation of a water film due to strong adhesion between liquid and
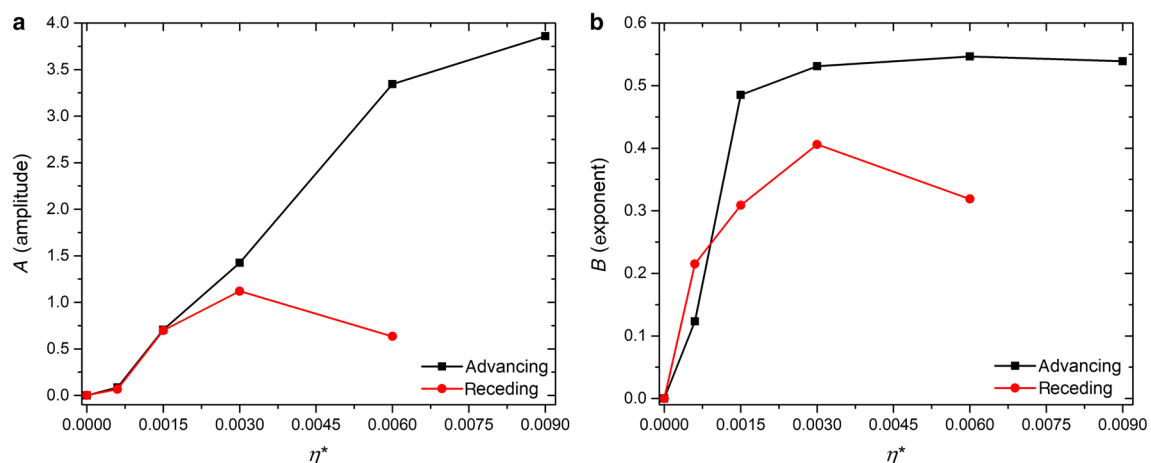
Fig. 12 Relationship between η^* and power-law fitting constants: **a** amplitude and **b** exponent
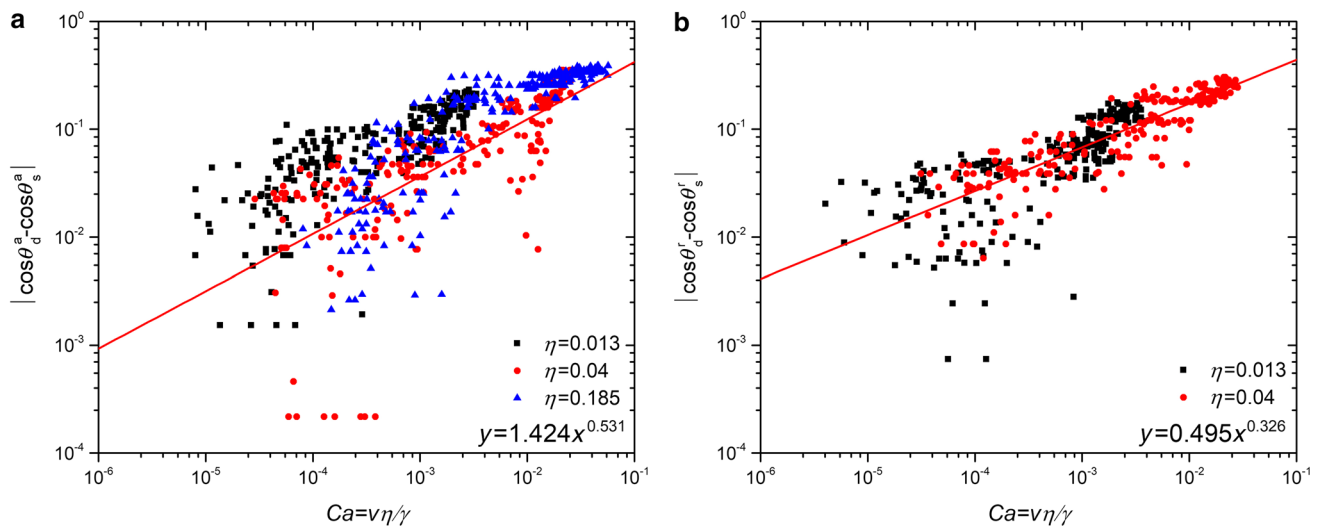
Fig. 13 Scatter plot of dynamic contact angles with different fluid viscosity and $\eta^*/\eta = 0.075$: **a** advancing angle; **b** receding angle

solid particles, as discussed with respect to Fig. 9. Therefore, the receding case with $\eta^* > 0.006$ Pa·s is not considered in the analysis of these results. It can be concluded from our simulations that the values of the power-law fitting constants, A and B, show a positive correlation with η^*. Note that, for any given η^*, predictions can be made for both the advancing and receding cases.

As stated in Sect. 3.2, to reproduce the dynamic contact angle, the viscosity η at the liquid–solid interface is replaced by the interfacial viscous force parameter η^*, which is related to the slip length and surface roughness at the microscopic scale. The above-mentioned simulations are conducted with the same fluid viscosity, and different power-law fitting parameters are derived depending on the value of η^*. However, for fluids with different viscosity, the prediction and dependence of the dynamic contact angle results on different values of η^* are unknown. From Eq. (18), it is seen that the ratio of the interfacial viscous force parameter η^* and the bulk viscosity η, i.e. η^*/η, dominates the power-law correlation between the dynamic contact angle and Ca, and the same value of η^*/η will reproduce similar results for fluids with different viscosity. To examine the influence of η^*/η on the dynamic contact angle simulation results, two additional sets of simulations with different bulk viscosity values (0.013 Pa·s and 0.185 Pa·s) are conducted, and the results compared with the cases with $\eta^* = 0.003$ Pa·s and $\eta = 0.04$ Pa·s discussed in Sect. 5.3. All three of these cases have the same value of $\eta^*/\eta = 0.075$.

The data cover the range of Ca from 10^{-6} to 10^{-1}, and the results are plotted in Fig. 12. The red line is the fitting function derived from the reference case with $\eta = 0.04$ Pa·s and $\eta^* = 0.003$ Pa·s. The dynamic receding case with fluid bulk viscosity of 0.185 Pa·s is excluded from this discussion, as in this high-viscosity setting the interfacial viscous force

F_i^{vis} will be quite large for fixed ratio η^*/η, causing the strong adhesion between liquid and solid particles discussed above, making the determination of accurate contact angles difficult.

Figure 13 shows that the scattered data of the three cases cover different ranges of Ca as the viscosity is varied. Nonetheless, the data for the advancing and receding cases with different bulk viscosity values can still be described by the reference curve. This result demonstrates that, for fluids with different viscosity, the same η^*/η ratio will lead to similar dynamic contact angle as well as corresponding power-law fitting results.

4 Conclusions

A modified SPH model with a newly introduced interfacial viscous force formulation is presented to simulate the rate-dependent behaviour of a moving contact line within a coarse-grained modelling approach. The dynamic contact angle is successfully reproduced using this implementation of the interfacial viscous force. Correlations between the simulated dynamic contact angle and Ca are examined based on empirical power-law functions, and the results are in good agreement with experimental findings and theoretical analyses. Furthermore, the parametric study demonstrates the dependence of the contact angle hysteresis and power-law fit on the magnitude of the interfacial viscosity, which can be further related to measurable physical quantities, viz. the slip length and microscopic surface roughness. Note that the empirical power law derived in this study is the result of model predictions instead of input information. This modified SPH model provides a simple and robust numerical solution to problems involving dynamic contact angle hysteresis, and can be applied for simulating multi-phase

interactions at meso-scale, e.g. multiphase flow in complex and deformable porous media. In addition, this approach is particularly beneficial when multiphase interactions with heterogeneous interfaces (characterised by spatial variation of the roughness and slip length) are considered in the simulation. The derived results can shed light on a variety of industrial and geological applications where dynamic capillary interactions play a key role.

References

1. Abriola, L.M., Pinder, G.F.: A multiphase approach to the modeling of porous media contamination by organic compounds: 1. Equation development. Water Resour. Res. **21**, 11–18 (1985)
2. Ran, Q.Q., Gu, X.Y., Li, S.L.: A coupled model for multiphase fluid flow and sedimentation deformation in oil reservoir and its numerical simulation. Acta Mech. Sin. **13**, 264–272 (1997)
3. Bandara, U.C., Palmer, B.J., Tartakovsky, A.M.: Effect of wettability alteration on long-term behavior of fluids in subsurface. Comput. Part. Mech. **3**, 277–289 (2016)
4. Gan, Y., Maggi, F., Buscarnera, G., et al.: A particle-water based model for water retention hysteresis. Geotech. Lett. **3**, 152–161 (2013)
5. Flores-Johnson, E.A., Wang, S., Maggi, F., et al.: Discrete element simulation of dynamic behaviour of partially saturated sand. Int. J. Mech. Mater. Des. **12**, 495–507 (2016)
6. Li, S., Liu, M., Hanaor, D., et al.: Dynamics of viscous entrapped saturated zones in partially wetted porous media. Transp. Porous Media **125**, 193–210 (2018)
7. Kiwi-Minsker, L., Renken, A.: Microstructured reactors for catalytic reactions. Catal. Today **110**, 2–14 (2005)
8. Schwartz, A.M., Tejada, S.B.: Studies of dynamic contact angles on solids. J. Colloid Interface Sci. **38**, 359–375 (1972)
9. Jiang, T.S., Soo-Gun, O.H., Slattery, J.C.: Correlation for dynamic contact angle. J. Colloid Interface Sci. **69**, 74–77 (1979)
10. Bracke, M., De Voeght, F., Joos, P.: The kinetics of wetting: the dynamic contact angle. Prog. Colloid Pol. Sci. **79**, 142–149 (1989)
11. Cox, R.G.: The dynamics of the spreading of liquids on a solid surface. Part 1. Viscous flow. J. Fluid Mech. **168**, 169–194 (1986)
12. Hoffman, R.L.: A study of the advancing interface: II. Theoretical prediction of the dynamic contact angle in liquid–gas systems. J. Colloid Interface Sci. **94**, 470–486 (1983)
13. Raiskinmäki, P., Shakib-Manesh, A., Jäsberg, A., et al.: Lattice-Boltzmann simulation of capillary rise dynamics. J. Stat. Phys. **107**, 143–158 (2002)
14. Koplik, J., Banavar, J.R., Willemsen, J.F.: Molecular dynamics of Poiseuille flow and moving contact lines. Phys. Rev. Lett. **60**, 1282–1285 (1988)
15. Huber, M., Keller, F., Säckel, W., et al.: On the physically based modeling of surface tension and moving contact lines with dynamic contact angles on the continuum scale. J. Comput. Phys. **310**, 459–477 (2016)
16. Lukyanov, A.V., Likhtman, A.E.: Dynamic contact angle at the nanoscale: a unified view. ACS Nano **10**, 6045–6053 (2016)
17. Tartakovsky, A.M., Panchenko, A.: Pairwise force smoothed particle hydrodynamics model for multiphase flow: surface tension and contact line dynamics. J. Comput. Phys. **305**, 1119–1146 (2016)
18. Eral, H.B., Oh, J.M.: Contact angle hysteresis: a review of fundamentals and applications. Colloid Polym. Sci. **291**, 247–260 (2013)
19. Rame, E.: The interpretation of dynamic contact angles measured by the Wilhelmy plate method. J. Colloid Interface Sci. **185**, 245–251 (1997)
20. Blake, T.D., Haynes, J.M.: Kinetics of liquid–liquid displacement. J. Colloid Interface Sci. **30**, 421–423 (1969)
21. Petrov, P., Petrov, I.: A combined molecular-hydrodynamic approach to wetting kinetics. Langmuir **8**, 1762–1767 (1992)
22. Elliott, G.E.P., Riddiford, A.C.: Dynamic contact angles: I. The effect of impressed motion. J. Colloid Interface Sci. **23**, 389–398 (1967)
23. Schäffer, E., Wong, P.Z.: Contact line dynamics near the pinning threshold: a capillary rise and fall experiment. Phys. Rev. E **61**, 5257–5277 (2000)
24. Shi, Z., Zhang, Y., Liu, M., et al.: Dynamic contact angle hysteresis in liquid bridges. Colloids Surf. A Physicochem. Eng. Asp. **555**, 365–371 (2018)
25. Kim, J.H., Rothstein, J.P.: Dynamic contact angle measurements of viscoelastic fluids. J. Nonnewton Fluid Mech. **225**, 54–61 (2015)
26. Seebergh, J.E., Berg, J.C.: Dynamic wetting in the low capillary number regime. Chem. Eng. Sci. **47**, 4455–4464 (1992)
27. Kordilla, J., Tartakovsky, A.M., Geyer, T.: A smoothed particle hydrodynamics model for droplet and film flow on smooth and rough fracture surfaces. Adv. Water Resour. **59**, 1–14 (2013)
28. Shigorina, E., Kordilla, J., Tartakovsky, A.M.: Smoothed particle hydrodynamics study of the roughness effect on contact angle and droplet flow. Phys. Rev. E **96**, 033115 (2017)
29. Meakin, P., Tartakovsky, A.M.: Modeling and simulation of pore-scale multiphase fluid flow and reactive transport in fractured and porous media. Rev. Geophys. **47**, RG3002 (2009)
30. Thompson, P.A., Robbins, M.O.: Simulations of contact-line motion: slip and the dynamic contact angle. Phys. Rev. Lett. **63**, 766–769 (1989)
31. Huang, P., Shen, L., Gan, Y., et al.: Coarse-grained modeling of multiphase interactions at microscale. J. Chem. Phys. **149**, 124505 (2018)
32. Dos Santos, L.O., Wolf, F.G., Philippi, P.C.: Dynamics of interface displacement in capillary flow. J. Stat. Phys. **121**, 197–207 (2005)
33. Chibbaro, S., Biferale, L., Diotallevi, F., et al.: Capillary filling for multicomponent fluid using the pseudo-potential lattice Boltzmann method. Eur. Phys. J. Spec. Top. **171**, 223–228 (2009)
34. Xu, A., Shyy, W., Zhao, T.: Lattice Boltzmann modeling of transport phenomena in fuel cells and flow batteries. Acta Mech. Sin. **33**, 555–574 (2017)
35. Chen, S., Doolen, G.D.: Lattice Boltzmann method for fluid flows. Annu. Rev. Fluid Mech. **30**, 329–364 (1998)
36. Bertrand, E., Blake, T.D., De Coninck, J.: Influence of solid–liquid interactions on dynamic wetting: a molecular dynamics study. J. Phys. Condens. Matter **21**, 464124 (2009)
37. Benzi, R., Biferale, L., Sbragaglia, M., et al.: Mesoscopic modeling of a two-phase flow in the presence of boundaries: the contact angle. Phys. Rev. E **74**, 021509 (2006)
38. Caiazzo, A.: Analysis of lattice Boltzmann nodes initialisation in moving boundary problems. Prog. Comput. Fluid Dyn. **8**, 3–10 (2008)
39. Tartakovsky, A., Meakin, P.: Modeling of surface tension and contact angles with smoothed particle hydrodynamics. Phys. Rev. E **72**, 026301 (2005)
40. Liu, M., Meakin, P., Huang, H.: Dissipative particle dynamics simulation of pore-scale multiphase fluid flow. Water. Resour. Res. **43**, W04411 (2007)
41. Li, L., Shen, L., Nguyen, G.D., et al.: A smoothed particle hydrodynamics framework for modelling multiphase interactions at meso-scale. Comput. Mech. **62**, 1071–1085 (2018)

42. Morris, J.P., Fox, P.J., Zhu, Y.: Modeling low Reynolds number incompressible flows using SPH. J. Comput. Phys. **136**, 214–226 (1997)

43. Becker, M., Teschner, M.: Weakly compressible SPH for free surface flows. In: Proceedings of the 2007 ACM SIGGRAPH/Eurographics Symposium on Computer Animation San Diego, California, 209–217 (2007)

44. Monaghan, J.J.: Simulating free surface flows with SPH. J. Comput. Phys. **110**, 399–406 (1994)

45. Breinlinger, T., Polfer, P., Hashibon, A., et al.: Surface tension and wetting effects with smoothed particle hydrodynamics. J. Comput. Phys. **243**, 14–27 (2013)

46. Monaghan, J.J.: Smoothed particle hydrodynamics. Annu. Rev. Astron. Astrophys. **30**, 543–574 (1992)

47. Liu, M.B., Liu, G.R.: Smoothed particle hydrodynamics (SPH): an overview and recent developments. Arch. Comput. Methods Eng. **17**, 25–76 (2010)

48. Meister, M., Burger, G., Rauch, W.: On the Reynolds number sensitivity of smoothed particle hydrodynamics. J. Hydraul. Res. **52**, 824–835 (2014)

49. Brackbill, J.U., Kothe, D.B., Zemach, C.: A continuum method for modeling surface tension. J. Comput. Phys. **100**, 335–354 (1992)

50. Monaghan, J.J., Kajtar, J.B.: SPH particle boundary forces for arbitrary boundaries. Comput. Phys. Commun. **180**, 1811–1820 (2009)

51. Colagrossi, A., Landrini, M.: Numerical simulation of interfacial flows by smoothed particle hydrodynamics. J. Comput. Phys. **191**, 448–475 (2003)

52. Feldman, J., Bonet, J.: Dynamic refinement and boundary contact forces in SPH with applications in fluid flow problems. Int. J. Numer. Methods Eng. **72**, 295–324 (2007)

53. Wang, J., Chan, D.: Frictional contact algorithms in SPH for the simulation of soil–structure interaction. Int. J. Numer. Anal. Methods Geomech. **38**, 747–770 (2014)

54. Schnell, E.: Slippage of water over nonwettable surfaces. J. Appl. Phys. **27**, 1149–1152 (1956)

55. Churaev, N.V., Sobolev, V.D., Somov, A.N.: Slippage of liquids over lyophobic solid surfaces. J. Colloid Interface Sci. **97**, 574–581 (1984)

56. Cheng, J.T., Giordano, N.: Fluid flow through nanometer-scale channels. Phys. Rev. E **65**, 031206 (2002)

57. Choi, C.H., Westin, K.J.A., Breuer, K.S.: Apparent slip flows in hydrophilic and hydrophobic microchannels. Phys. Fluids **15**, 2897–2902 (2003)

58. Pit, R., Hervet, H., Leger, L.: Direct experimental evidence of slip in hexadecane: solid interfaces. Phys. Rev. Lett. **85**, 980–983 (2000)

59. Rothstein, J.P.: Slip on superhydrophobic surfaces. Annu. Rev. Fluid Mech. **42**, 89–109 (2010)

60. Majumder, M., Chopra, N., Andrews, R., et al.: Nanoscale hydrodynamics: enhanced flow in carbon nanotubes. Nature **438**, 44–44 (2005)

61. Lee, C., Kim, C.J.C.: Maximizing the giant liquid slip on superhydrophobic microstructures by nanostructuring their sidewalls. Langmuir **25**, 12812–12818 (2009)

62. Ramachandran, P.: A reproducible and high-performance framework for smoothed particle hydrodynamics. In: Proceedings of the 15th Python in Science Conference, pp. 127–135 (2016)

63. Liu, G.R., Liu, M.B.: Smoothed Particle Hydrodynamics: A Meshfree Particle Method. World Scientific, Singapore (2003)

64. Hocking, L.M.: A moving fluid interface on a rough surface. J. Fluid Mech. **76**, 801–817 (1976)

65. Niavarani, A., Priezjev, N.V.: Modeling the combined effect of surface roughness and shear rate on slip flow of simple fluids. Phys. Rev. E **81**, 011606 (2010)

66. Thompson, P.A., Troian, S.M.: A general boundary condition for liquid flow at solid surfaces. Nature **389**, 360–362 (1997)

67. Karim, A.M., Rothstein, J.P., Kavehpour, H.P.: Experimental study of dynamic contact angles on rough hydrophobic surfaces. J. Colloid Interface Sci. **513**, 658–665 (2018)

68. Landau, L.D., Levich, B.: Dynamics of Curved Fronts. Academic, San Diego (1988)

69. Li, X., Fan, X., Askounis, A., et al.: An experimental study on dynamic pore wettability. Chem. Eng. Sci. **104**, 988–997 (2013)